

On-site calibration method for outdoor binocular stereo vision sensors



Zhen Liu^{*}, Yang Yin, Qun Wu, Xiaojing Li, Guangjun Zhang

Key Laboratory of Precision Opto-mechatronics Technology, Ministry of Education, Beihang University, No. 37 Xueyuan Rd, Haidian District, 100191 Beijing, PR China

ARTICLE INFO

Article history:

Received 11 January 2016

Received in revised form

19 April 2016

Accepted 17 May 2016

Available online 30 May 2016

Keywords:

Calibration

Stereo vision sensor

Line laser projector

Outdoor environments

ABSTRACT

Using existing calibration methods for binocular stereo vision sensors (BSVS), it is very difficult to extract target characteristic points in outdoor environments under complex light conditions. To solve the problem, an online calibration method for BSVS based a double parallel cylindrical target and a line laser projector is proposed in this paper. The intrinsic parameters of two cameras are calibrated offline. Laser strips on the double parallel cylindrical target are mediated to calibrate the configuration parameters of BSVS. The proposed method only requires images of laser strips on the target and is suitable for the calibration of BSVS in outdoor environments. The effectiveness of the proposed method is validated through physical experiments.

© 2016 Elsevier Ltd. All rights reserved.

1. Introduction

Stereoscopic vision inspection is widely utilized in industrial measurement [1–4]. And there always exist complicated conditions in outdoor environments such as complex light condition, bad weather condition, and strong vibration and so on. In order to be adaptive for these conditions, binocular stereo vision sensors (BSVS) usually have protections, including rugged protective shells and optical protective equipment to remove external inference of light, such as optical filters. Meanwhile, many users ask for simple and fast method to calibrate BSVS. For example, BSVS installed on the both sides of railway lines for detecting the size and fault of vehicle, are requested for working all days. The less time maintenance and calibration occupy, the more time BSVS can work. Besides, the high calibration accuracy is not particularly demanded. The calibration accuracy of 0.05 mm is good enough to meet measurement requirements. As a result, the fast and simple calibration with moderate accuracy is required for this kind of BSVS. Existing online calibration of BSVS in outdoor environments under strong or weak light often presents difficulties. Thus, exploring the high-precision calibration of BSVS in outdoor measurement environments is significant.

BSVS calibration is divided into two parts, namely, calibration of the intrinsic parameters of two cameras and calibration of the coordinate transformation matrix between two cameras; the latter is also called configuration parameter calibration of BSVS. Intrinsic

parameter calibration of a camera is relatively mature, and existing methods for this type of calibration rely on different types of targets, such as 3D [5,6], 2D [7,8], 1D [9,10], and sphere [11–13] targets. Among these methods, the calibration method proposed by Zhang [7] using a 2D target is the most popular. The method has high flexibility, high accuracy, and several other advantages. When 3D, 2D, and sphere targets are utilized for the calibration of the two cameras intrinsic parameters of BSVS, the two cameras capture the images of the target at the same time, and the transformation matrix between coordinate frames of the two cameras can be obtained. For 3D and 2D targets, the accuracy of the calibration of camera intrinsic parameters and configuration parameters of BSVS is relatively higher than that of other targets. However, for sphere targets, none of the existing methods satisfy the high-precision measurement requirements. Reference [10] shows that a single 1D target without constraints cannot realize intrinsic parameter calibration of a camera; however, the configuration parameters of BSVS can be obtained [14] with known intrinsic parameters of two cameras of BSVS and the known distance between characteristic points of the 1D target. A 1D target is suitable for configuration parameter calibration of a wide-field BSVS.

As for the camera calibration in outdoor environments, some methods have been brought forward. In references [15,16], Dawson and Zheng utilize vanishing points and vanishing lines to calibrate practical traffic cameras. This method can be applied to practical traffic cameras well, because features of vanishing points and vanishing lines such as parallel road boundaries and walking human, can be obtained from traffic surveillance images. Tian [17] proposes a calibration method for large field vision in outdoor environments. In the experiments, three independent targets

^{*} Corresponding author.

E-mail address: liuzhen008@buaa.edu.cn (Z. Liu).

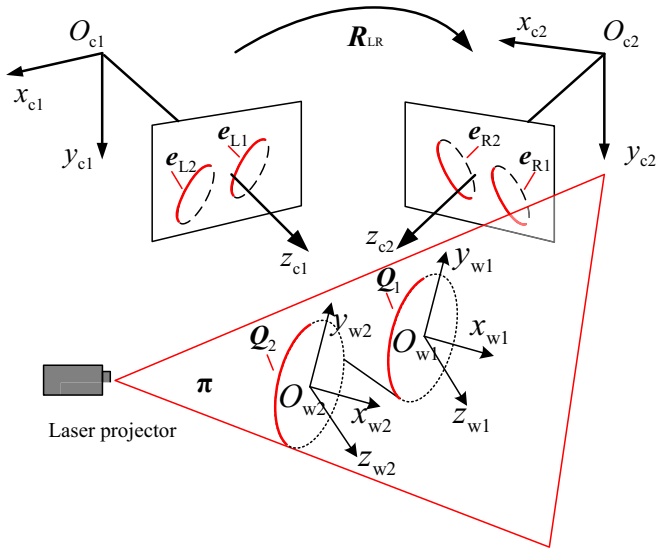


Fig. 1. Configuration parameter calibration of BSVS.

which have the same height are set in the field to calibrate cameras. And Liu [18] introduces an outdoor binocular camera calibration method for a multi-GPS apparatuses and multi-cameras. To calibrate the binocular camera in an outdoor environment, the Scale Invariant Feature Transform (SIFT) descriptor is used to compute the features in images. In purpose of avoiding the impacts of the sun light, all the cameras in experiments should be fixed at a proper position. Also, an adaptive optical band pass filter is designed for the measurement system in reference [19] to get clear images under complex background light conditions. However, adding an optical filter in front of the camera lens increases the difficulty of online calibration. Optical filters should be removed before calibrations. All the above methods require clear features in images to complete calibrations, and the calibration accuracy of them is not high. When it comes to situations, however, such as foggy weather, reflect sunlight, strong sunlight and so on, their performances have been affected. Rodríguez [20] proposes a method based on laser line imaging and also uses Genetic Algorithm (GA) to calibrate and recalibrate the binocular setup without references and physical measurements. The laser projector has a stable light source and is actively irradiated on objects, which can solve the problem of obtaining clear features efficiently. In addition, this method has an advantage of high calibration accuracy without references and physical measurements. But, two cameras are supposed to keep parallel with the surface while the laser line projector is projected perpendicularly to the surface. Besides, the laser line projector and both two cameras are fixed on a high precision slider during the process of calibration and measurement. According to these experimental conditions, this method is more suitable for BSVS working in the indoor

environments rather than in the outdoor environments.

As a result, a novel online calibration method that only requires images of laser strips on a double parallel cylindrical target is proposed in this paper. Zhang's method is adopted to calibrate intrinsic parameters of two cameras offline, and configuration parameter calibration is achieved with the proposed method. The contents of this paper are structured as follows: Section 2 describes the basic principle of the algorithm in detail; Section 3 contains the information about physical experiment; and Section 4 presents the conclusion.

2. Algorithm principle

As shown in Fig. 1, $O_{c1}x_{c1}y_{c1}z_{c1}$ and $O_{c2}x_{c2}y_{c2}z_{c2}$ denote the coordinate frames of cameras 1 and 2, respectively. Q_j ($j = 1, 2$) denote two space ellipses of two laser strips on the target. e_{Lj} and e_{Rj} are images of two space ellipses on the image planes of the left and right cameras, respectively. The long axis of Q_1 is defined as the x -axis of $O_1x_1y_1z_1$, and the short axis is defined as the y -axis. The center of Q_1 is the origin of $O_1x_1y_1z_1$. Through a similar method, the coordinate frame of Q_2 , $O_2x_2y_2z_2$, can be obtained. We assume that $O_1x_1y_1z_1$ is the target coordinate frame $O_Tx_Ty_Tz_T$. R_{L1} and t_{L1} denote the rotation matrix and the translation vector from $O_1x_1y_1z_1$ to $O_{c1}x_{c1}y_{c1}z_{c1}$, respectively. R_{R1} and t_{R1} denote the rotation matrix and the translation vector from $O_1x_1y_1z_1$ to $O_{c2}x_{c2}y_{c2}z_{c2}$, respectively. R_{LR} and t_{LR} denote the rotation matrix and the translation vector from $O_{c1}x_{c1}y_{c1}z_{c1}$ to $O_{c2}x_{c2}y_{c2}z_{c2}$, respectively.

Given that the two cylinders of the target are parallel to each other and have the same diameter, the following conclusions can be obtained: the long and short axes of Q_1 and Q_2 are parallel and similar, and the short axis is equal to the diameter of the cylinder. Zhang's method [7] is adopted to calibrate the intrinsic parameters of two cameras offline. Eq. (1) is the camera model.

$$\rho p = \rho \begin{bmatrix} u \\ v \\ 1 \end{bmatrix} = K_L \begin{bmatrix} r_1 & r_2 & t_j \end{bmatrix} \begin{bmatrix} x \\ y \\ 1 \end{bmatrix} = H_{Lj} q \quad (1)$$

where ρ denotes a nonzero constant, $p = [u \ v \ 1]^T$ denotes the undistorted homogeneous coordinate under the image coordinate frame of the left camera, $q = [x \ y \ 1]^T$ denotes the 2D coordinate on $O_Tx_Ty_T$, K_L denotes the intrinsic parameter matrix of the left camera, and $R_{Lj} = [r_1 \ r_2 \ r_3]$ and t_{Lj} denote the rotation matrix and translation vector from $O_jx_jy_jz_j$ to $O_{c1}x_{c1}y_{c1}z_{c1}$, respectively. Since $O_1x_1y_1z_1$ and $O_2x_2y_2z_2$ is parallel, $R_{L1} = R_{L2}$. e_{Lj} and Q_j can be expressed by Eq. (2).

$$\begin{cases} p^T e_{Lj} p = 0 \\ q^T Q_j q = 0 \end{cases} \quad (2)$$

where $Q_j = \begin{pmatrix} 1/b^2 & 0 & 0 \\ 0 & 1/a^2 & 0 \\ 0 & 0 & -1 \end{pmatrix}$ and $2b$ denotes the long axis of the



Fig. 2. Images of different targets captured by the vision sensor under good light conditions.

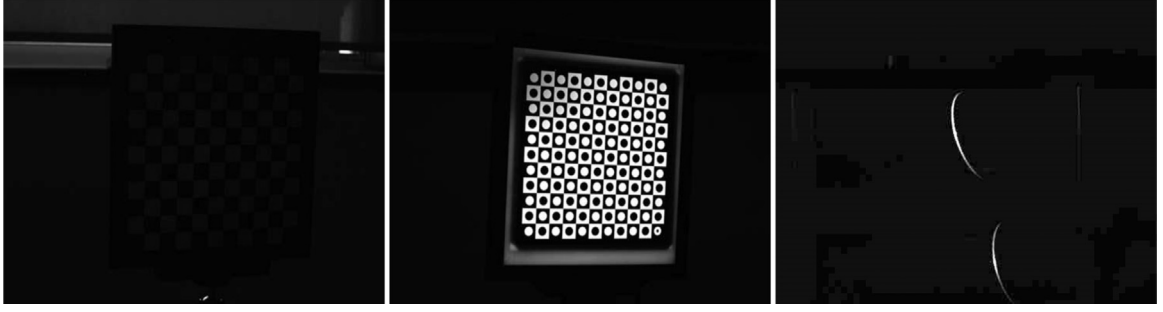


Fig. 3. Images of different targets captured by the vision sensor under dim light conditions.

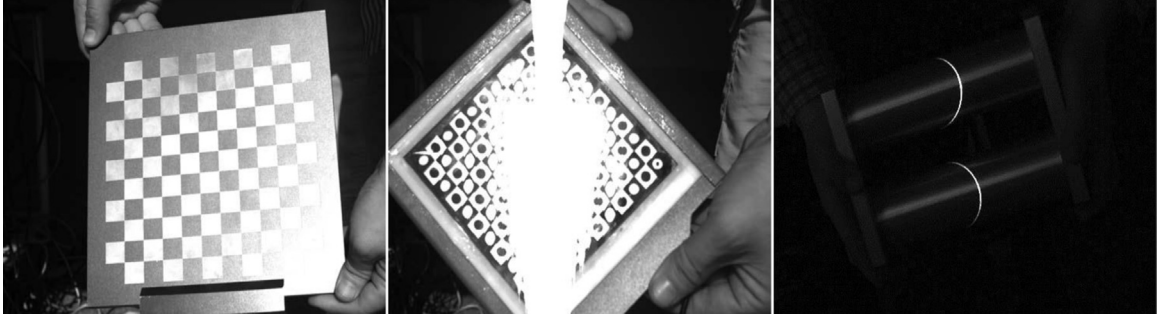


Fig. 4. Images of different targets captured by the vision sensor under strong sunlight conditions.



Fig. 5. Images of different targets captured by the vision sensor with an optical filter.

space ellipse, while $2a$ denotes the short axis that is equal to the diameters of the cylinder.

Combining Eqs. (1) and (2) results in:

$$\rho_j \mathbf{Q}_j = \mathbf{H}_{ij}^T \mathbf{e}_{ij} \mathbf{H}_{ij} \quad (3)$$

where $\mathbf{H}_{ij} = \mathbf{K}_L [\mathbf{r}_1 \ \mathbf{r}_2 \ \mathbf{t}_j]$ and ρ_j denotes a non-zero scale factor.

The equation for the relation between \mathbf{e}_{ij} and \mathbf{Q}_j is expressed by Eq. (4).

$$\begin{pmatrix} 1/b^2 & 0 & 0 \\ 0 & 1/a^2 & 0 \\ 0 & 0 & -1 \end{pmatrix} = \begin{pmatrix} \mathbf{r}_1^T \mathbf{W}_j \mathbf{r}_1 & \mathbf{r}_1^T \mathbf{W}_j \mathbf{r}_2 & \mathbf{r}_1^T \mathbf{W}_j \mathbf{t}_j \\ \mathbf{r}_2^T \mathbf{W}_j \mathbf{r}_1 & \mathbf{r}_2^T \mathbf{W}_j \mathbf{r}_2 & \mathbf{r}_2^T \mathbf{W}_j \mathbf{t}_j \\ \mathbf{t}_j^T \mathbf{W}_j \mathbf{r}_1 & \mathbf{t}_j^T \mathbf{W}_j \mathbf{r}_2 & \mathbf{t}_j^T \mathbf{W}_j \mathbf{t}_j \end{pmatrix} \quad (4)$$

where $\mathbf{W}_j = \mathbf{K}_i^T \mathbf{e}_{ij} \mathbf{K}_i$.

Twelve separate equations are obtained from Eq. (4). \mathbf{R}_{L1} , \mathbf{t}_1 and \mathbf{t}_2 are determined to be unknown quantities, and contain nine unknown quantities. b , ρ_1 and ρ_2 are also unknown quantities. Thus, there are twelve unknown quantities. Given that Eq. (4) provides twelve equations, \mathbf{R}_{L1} and \mathbf{t}_{L1} can be solved according to the properties of \mathbf{r}_1 and \mathbf{r}_2 , $\mathbf{r}_1^T \mathbf{r}_1 = 1$; $\mathbf{r}_2^T \mathbf{r}_2 = 1$; $\mathbf{r}_1^T \mathbf{r}_2 = 0$.

Likewise, \mathbf{R}_{R1} and \mathbf{t}_{R1} can also be solved. \mathbf{R}_{LR} and \mathbf{t}_{LR} are solved with Eq. (5).

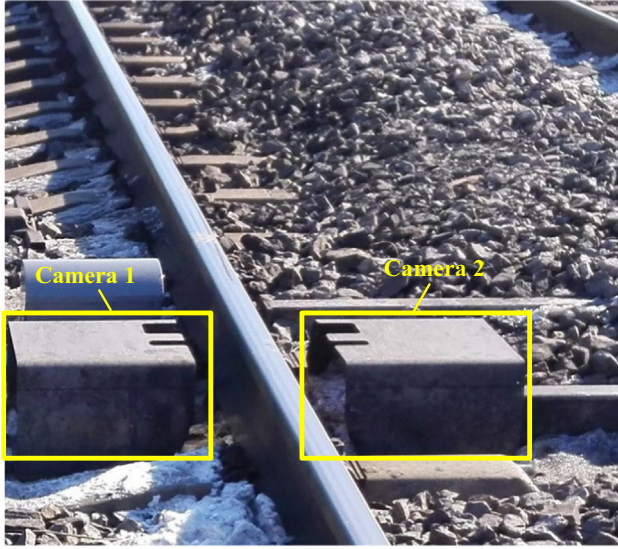
$$\begin{bmatrix} \mathbf{R}_{LR} & \mathbf{t}_{LR} \\ \mathbf{0} & 1 \end{bmatrix} = \begin{bmatrix} \mathbf{R}_{R1} & \mathbf{t}_{R1} \\ \mathbf{0} & 1 \end{bmatrix} \begin{bmatrix} \mathbf{R}_{L1} & \mathbf{t}_{L1} \\ \mathbf{0} & 1 \end{bmatrix}^{-T} \quad (5)$$

\mathbf{p}_L and \mathbf{p}_R are image points of P on the image planes of the left and right cameras, and their corresponding undistorted homogeneous image points are $\tilde{\mathbf{p}}_L$ and $\tilde{\mathbf{p}}_R$, respectively. The 3D coordinate of P in $O_{c1}x_{c1}y_{c1}z_{c1}$, $\mathbf{q}_L = (x_L, y_L, z_L, 1)^T$, can be obtained with Eq. (6) as follows:

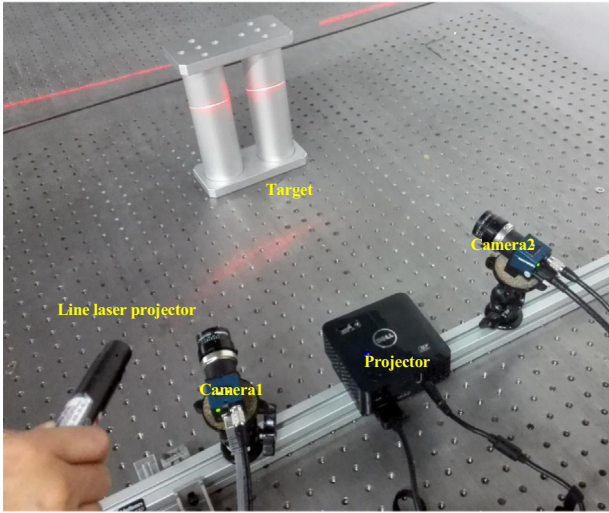
$$\begin{cases} \rho_L \tilde{\mathbf{p}}_L = \mathbf{K}_L [\mathbf{I}_{3 \times 3} \ \mathbf{0}_{3 \times 1}] \mathbf{q}_L \\ \rho_R \tilde{\mathbf{p}}_R = \mathbf{K}_R [\mathbf{R}_{LR} \ \mathbf{t}_{LR}] \mathbf{q}_L \end{cases} \quad (6)$$

where ρ_L, ρ_R are non-zero constants.

At the i th placement of the double parallel cylinder target, the image centers of laser strips on the target are extracted, and their image distortions are corrected [7]. We assume that the undistorted homogeneous image coordinates of the m th point of laser strips in the image coordinate frames of the left and right cameras are $\tilde{\mathbf{p}}_{Li(m)}$ and $\tilde{\mathbf{p}}_{Ri(m)}$, respectively. Based on \mathbf{R}_{L1i} , \mathbf{t}_{L1i} , \mathbf{R}_{LR} and \mathbf{t}_{LR} , \mathbf{H}_{L1i} and \mathbf{H}_{R1i} are solved. The 2D coordinates of $\tilde{\mathbf{p}}_{Li(m)}$ and $\tilde{\mathbf{p}}_{Ri(m)}$ on $O_T x_T y_T$, $\mathbf{q}_{Li(m)}$ and $\mathbf{q}_{Ri(m)}$ are solved with Eq. (1). Based on $\mathbf{q}_{Li(m)}$, the short axes $[A_{1i(L)} \text{ and } A_{2i(L)}]$, long axes $[B_{1i(L)} \text{ and } B_{2i(L)}]$, $\mathbf{o}_{1i(L)}(x_{1i(L)}, y_{1i(L)})$, and $\mathbf{o}_{2i(L)}(x_{2i(L)}, y_{2i(L)})$ of \mathbf{Q}_{Li} and \mathbf{Q}_{2i} are obtained by ellipse fitting. Likewise, based on $\mathbf{q}_{Ri(m)}$, the short axes $[A_{1i(R)}$



(a). Measurement system in a complex illumination condition



(b). 3D scanner and the double parallel cylinder target in the physical experiment

Fig. 6. (a) Measurement system in a complex illumination condition. (b) 3D scanner and the double parallel cylinder target in the physical experiment.

and $A_{2i(R)}$], long axes $[B_{1i(R)}$ and $B_{2i(R)}$], $\mathbf{o}_{1i(R)}(x_{1i(R)}, y_{1i(R)})$, and $\mathbf{o}_{2i(R)}(x_{2i(R)}, y_{2i(R)})$ of \mathbf{Q}_{1i} and \mathbf{Q}_{2i} are obtained by ellipse fitting. In theory, $x_{1i(L)} = y_{1i(L)} = x_{1i(R)} = y_{1i(R)} = 0$.

The objective functions are established as follows:

$$f(\alpha) = \min \left(\sum_{i=1}^n \left(\begin{aligned} &|A_{1i(L)} - 2a| + |A_{2i(L)} - 2a| + |A_{1i(R)} - 2a| \\ &+ |A_{2i(R)} - 2a| + |B_{1i(L)} - B_{2i(L)}| \\ &+ |B_{1i(R)} - B_{2i(R)}| + x_{1i(L)} + y_{1i(L)} + x_{1i(R)} \\ &+ y_{1i(R)} + (x_{2i(L)} - x_{2i(R)}) + (y_{2i(L)} - y_{2i(R)}) \end{aligned} \right) \right) \quad (7)$$

where $\alpha = (\mathbf{R}_{LR}, \mathbf{t}_{LR}, \mathbf{R}_{L1i}, \mathbf{t}_{L1i})$, $i = 1, 2, \dots, n$, and n denotes the placement number of the target. The optimum solution of α is obtained with the nonlinear optimization method [21].

3. Physical experiment

The physical experiment has three sections. Firstly, it is validated that the proposed method shows superior effects in outdoor

environments under complex light conditions. Then, in the second section, it shows the calibration accuracy of the proposed method. Moreover, the practical applications of the proposed method are displayed in the third section.

3.1. The performance evaluations of different targets under complex light conditions

As shown in Fig. 2, three targets, namely, the common planar, light-emitting planar, and double parallel cylinder targets, have clear target images under good light conditions. Common and light-emitting planar targets are prone to have strong light reflection under strong light conditions (Fig. 4). By contrast, it is difficult for the common target to obtain a clear image of characteristic points under weak light conditions but easy for the light-emitting target to obtain a clear image of characteristic points (Fig. 3). The vision sensor with an optical filter cannot obtain any information on characteristic points from the image when the common planar and light-emitting planar targets are utilized (Fig. 5).

As shown in Figs. 2–5, the proposed method can always obtain a clear image of the laser strip on the target. The above analysis validates the good performance of the proposed method under complex light conditions.

3.2. The calibration accuracy evaluation

A complex illumination condition in which the proposed calibration method is widely used is shown in Fig. 6(a). As shown in Fig. 6(a), we can see that the measurement system consists of two cameras with rugged protective shells and they are installed on the both sides of the railway line. And in order to better compare the proposed method with Zhang's method, we carry out the experiments in the environment as shown in Fig. 6(b). Two cameras of the system are the same model. The image resolution of the cameras is 1628 pixels \times 1236 pixels, the field of view is approximately 200 mm \times 200 mm \times 170 mm. A 3D scanner consisting of a projector and BSVS is used to evaluate the validity of the proposed method.

The proposed method is compared with Zhang's method [6,22] in the physical experiment, and the calibration accuracy of the proposed method is verified. First, the intrinsic parameters calibration of two cameras and configuration parameter calibration of BSVS are completed with Zhang's method [6,22]. Second, based on the results of the calibration of the intrinsic parameters of two cameras, the proposed method is adopted to calibrate the configuration parameters of BSVS.

The intrinsic parameter calibration results of the two cameras obtained with Zhang's method are shown below.

Intrinsic parameters of camera 1: $f_x=4000.51$; $f_y=4000.13$; $\gamma = -1 \times 10^{-5}$; $u_0=819.38$; $v_0=609.19$; $k_1=-0.26$; $k_2=0.53$

Intrinsic parameters of camera 2: $f_x=4003.69$; $f_y=4003.46$; $\gamma = 6 \times 10^{-5}$; $u_0=822.20$; $v_0=612.18$; $k_1=-0.25$; $k_2=0.50$

In the calibration of the configuration parameters of BSVS, the diameter of the double parallel cylinder target is 60 mm, with an accuracy of 0.02 mm; the number of characteristic points of the light-emitting planar target is 10×10 , with an accuracy of 5 μm . The number of times that the two targets are subjected to calibration is 15. The images captured by the vision sensor are shown in Fig. 7. Based on the method proposed by Steger in reference [23], the peak points of laser strips are obtained. This extraction method has advantages of good accuracy and robustness. \mathbf{R}_{LR} and \mathbf{t}_{LR} obtained with Zhang's method:

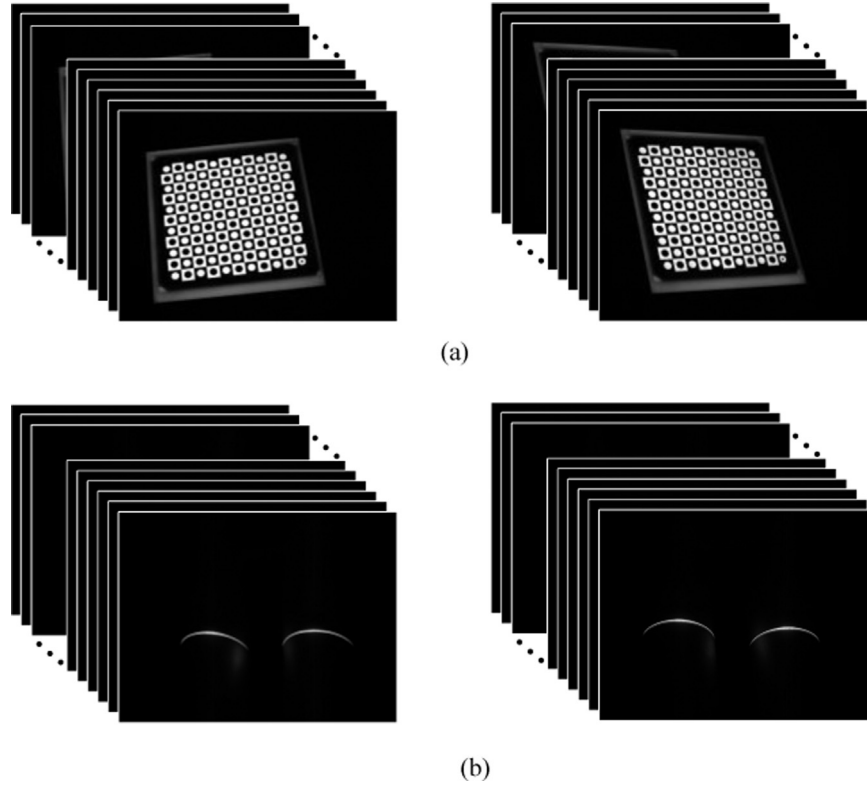


Fig. 7. Target images captured by the two cameras. (a) Images of the light-emitting planar target captured by the two cameras. (b) Images of the double parallel cylinder target captured by the two cameras.

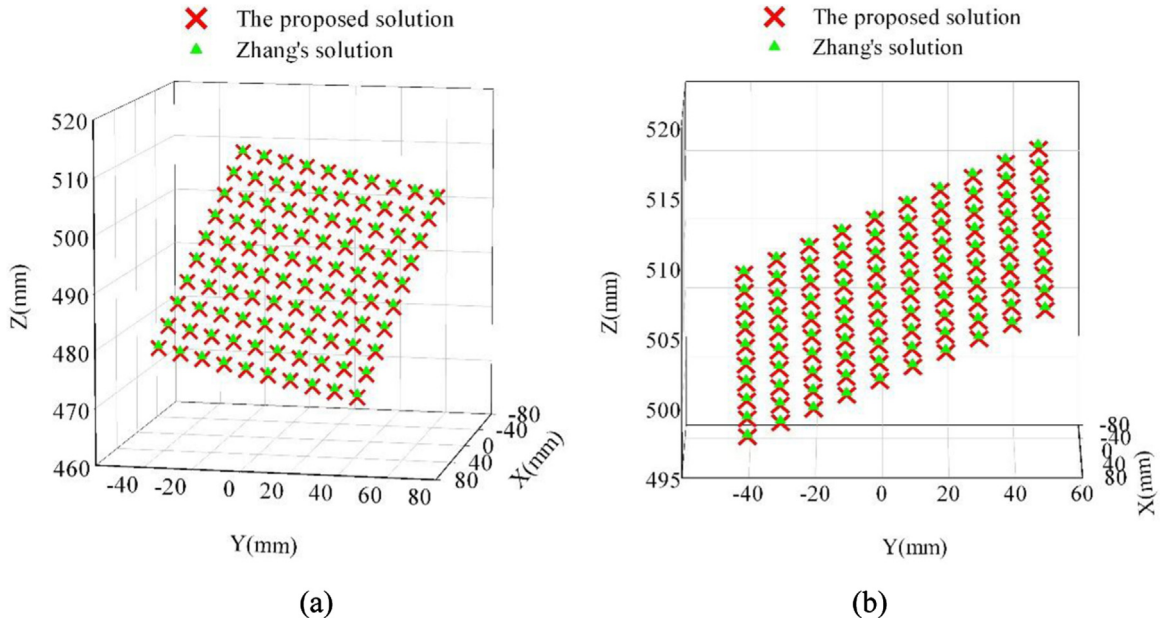


Fig. 8. Measurement results of two calibration results. (a) Measurement results of the first placement and (b) measurement results of the second placement. (For interpretation of the references to color in this figure, the reader is referred to the web version of this article.)

$$\mathbf{R}_{\text{LR}} = \begin{bmatrix} 0.902 & -0.093 & -0.421 \\ 0.095 & 0.995 & -0.017 \\ 0.421 & -0.025 & 0.907 \end{bmatrix}, \mathbf{t}_{\text{LR}} = \begin{bmatrix} 233.03 \\ 4.50 \\ 46.44 \end{bmatrix}$$

\mathbf{R}_{LR} and \mathbf{t}_{LR} obtained with the proposed method:

$$\mathbf{R}_{\text{LR}} = \begin{bmatrix} 0.904 & -0.094 & -0.416 \\ 0.097 & 0.995 & -0.015 \\ 0.415 & -0.027 & 0.909 \end{bmatrix}, \mathbf{t}_{\text{LR}} = \begin{bmatrix} 230.15 \\ 3.27 \\ 45.91 \end{bmatrix}$$

The light-emitting planar target is placed for two times in front of BSVS. The 3D coordinates of characteristic points of the light-emitting planar target are obtained based on the results of Zhang's method and the proposed method. As shown in Fig. 8, the green crosses are the results of using Zhang's method and the red marks are the results of using the proposed method. The 3D coordinates of ten testing points in measurement results are shown in Table 1.

The distance between any two testing points in Table 1 are calculated as the measurement distance d_m . And the distance

Table 1
3D coordinates of the testing points obtained using different calibration results (mm).

Index		Zhang's method			Proposed method		
		x	y	z	x	y	z
First position	1	16.83	−47.09	477.10	16.82	−46.96	476.61
	2	21.16	−27.61	475.76	21.15	−27.48	475.24
	3	25.49	−8.13	474.43	25.47	−8.01	473.88
	4	29.83	11.35	473.12	29.80	11.46	472.54
	5	34.16	30.84	471.81	34.13	30.93	471.20
Second position	1	37.89	−40.62	497.10	37.89	−40.55	496.93
	2	18.00	−40.96	499.25	18.00	−40.87	499.03
	3	−1.88	−41.31	501.41	−1.87	−41.22	501.16
	4	−21.76	−41.66	503.58	−21.74	−41.55	503.32
	5	−41.64	−42.01	505.78	−41.60	−41.89	505.53

Table 2
RMS errors of the testing points using different calibration results (mm).

Index		Zhang's method			Proposed method		
		d_m · (mm)	d_t · (mm)	Δd · (mm)	d_m · (mm)	d_t · (mm)	Δd · (mm)
First position	1	20.01	20.00	0.01	20.01	20.00	0.01
	2	40.01	40.00	0.01	40.00	40.00	0.00
	3	60.00	60.00	0.00	59.98	60.00	0.02
	4	80.01	80.00	0.01	79.97	80.00	0.03
Second position	1	20.01	20.00	0.01	20.00	20.00	0.00
	2	40.01	40.00	0.01	39.99	40.00	0.01
	3	60.02	60.00	0.02	59.98	60.00	0.02
	4	80.01	80.00	0.01	79.97	80.00	0.03
RMS errors				0.01			0.02

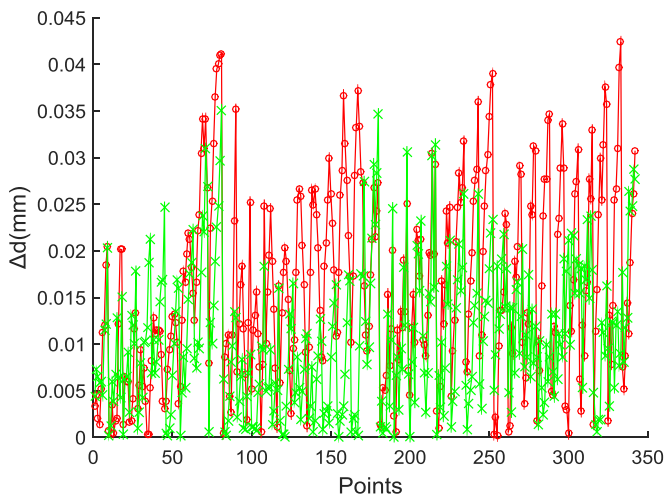


Fig. 9. Target points obtained with the two calibration methods. (For interpretation of the references to color in this figure, the reader is referred to the web version of this article.)

between the first testing point and the remaining four testing points is calculated at each position via two methods. The distance between any two testing points in the coordinate frame of the light-emitting planar target is calculated as the ideal distance d_t . As shown in Table 2, the errors of the measurement experiments which is represented by the errors of the distance between the testing points, are obtained using Eq. (8).

$$\Delta d = |d_m - d_t| \quad (8)$$

The RMS errors of ten testing points, which is described by the RMS of all the Δd in Table 2, via Zhang's method and the proposed method is 0.01 mm and 0.02 mm, respectively.

Similarly, RMS errors are obtained by comparing the measured distance and actual distance between all arbitrary two points of the light-emitting planar target. As shown in Fig. 9, the green points are the errors Δd of using Zhang's method, and the red points are that using the proposed method. The X axis denotes the sequence of points while the Y axis denotes the deviation Δd of each point between d_m and d_t . The RMS error is obtained by estimating the RMS of all the Δd . And the RMS errors obtained with two calibration results of Zhang's method and the proposed method are 0.01 mm and 0.02 mm, respectively.

The metal workpiece (It has two parallel planes, the distance of which is 60 mm) is measured based on the two calibration methods. As shown in Fig. 10(a), the measurement result based on Zhang's method is denoted by green points and that based on the proposed method is denoted by red points. The measurement error is also described by the deviation Δd between d_m and d_t . Here, d_m is the distance between planes reconstructed by the calibration result while d_t is the distance between planes which is known as machined. The measurement errors of Zhang's method and the proposed method are 0.02 mm and 0.03 mm, respectively. As shown in Fig. 10(b), it is the actual picture of the mental workpiece.

3.3. Application results of the proposed method

In order to validate the effectiveness of the proposed method, a toy gun and Venus statue are measured by 3D scanner calibrated by the proposed method. Measurement results of the toy gun and Venus statue are shown in Fig. 11(a) and (b), respectively.

4. Conclusion

Compared with existing calibration methods for BSVS, the proposed method does not require characteristic points or contour

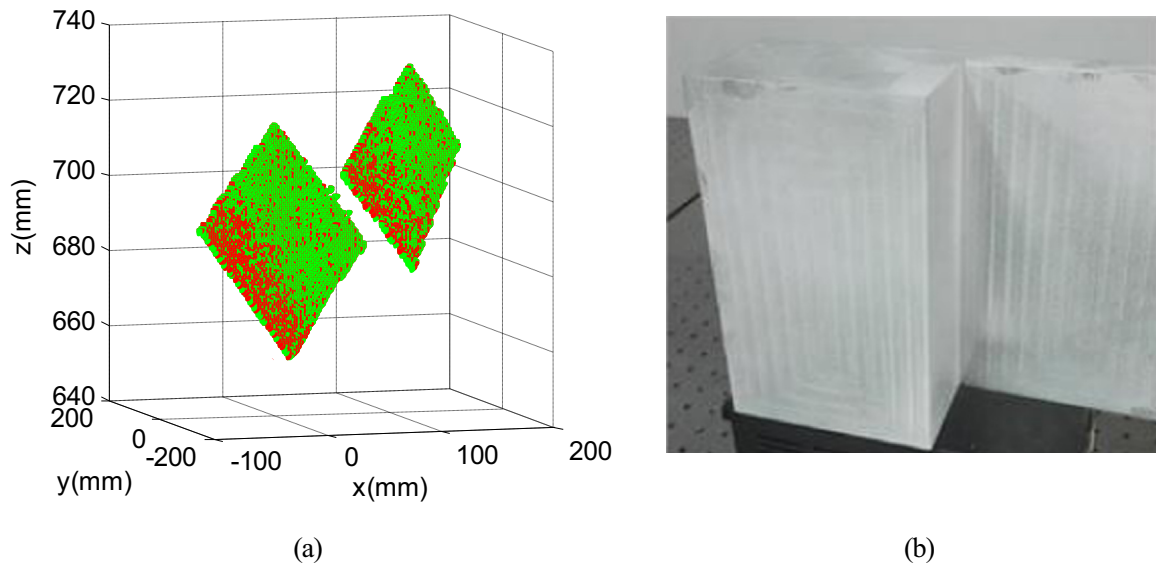


Fig. 10. Measurement results obtained with the two calibration methods of metal workpiece. (a) Measurement results obtained with the two calibration methods and (b) metal workpiece. (For interpretation of the references to color in this figure, the reader is referred to the web version of this article.)

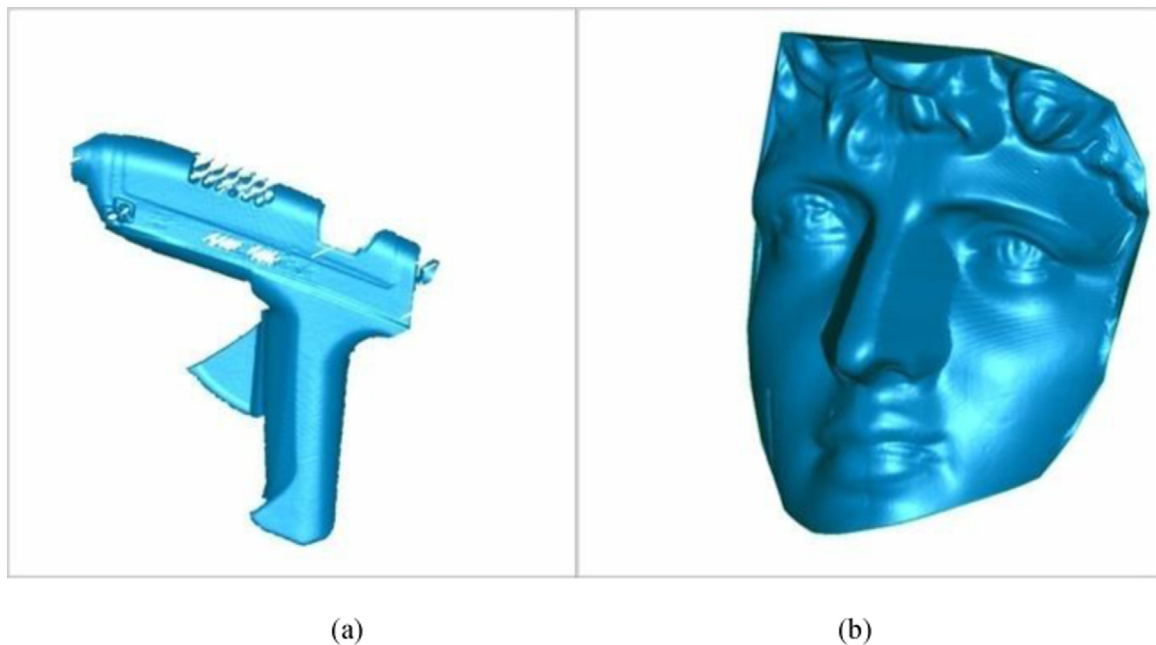


Fig. 11. Measurement results of the toolbox and Venus statue. (a) Measurement results of the toy gun and (b) measurement results of Venus statue.

information of the target and is suitable for online calibration of BSVS under complex light conditions and even for online calibration of BSVS with an optical filter. The double parallel cylinder target is easy to machine at low costs and has high machine accuracy. The experiments verify that when the field of view of BSVS is approximately $200 \text{ mm} \times 200 \text{ mm} \times 170 \text{ mm}$, the proposed method can achieve a stated accuracy of up to 0.02 mm , which is equivalent to the calibration result using the planar target.

Acknowledgment

The authors acknowledge the support from National Natural Science Foundation of China under Grant no. 51575033, 51175027 and the Beijing Natural Science Foundation under Grant no. 3132029.

References

- [1] Malamas E, Petrakis E, Zervakis M, Petit L, Legat J. A survey on industrial vision systems, applications and tools. *Image Vis Comput* 2003;21(2):171–88.
- [2] Zhang S. Recent progresses on real-time 3D shape measurement using digital fringe projection techniques. *Opt Laser Eng* 2010;48(2):149–58.
- [3] Shirmohammadi S, Ferrero A. Camera as the instrument: the rising trend of vision based measurement. *IEEE Trans Instrum Meas* 2014;17(3):41–7.
- [4] Chen F, Brown GM, Song M. Overview of three-dimensional shape measurement using optical methods. *Opt Eng* 2000;39(1):10–22.
- [5] Tsai RY. A versatile camera calibration technique for high-accuracy 3D machine vision metrology using off-the-shelf TV cameras and lenses. *IEEE J Robot Autom* 1987;3(4):323–44.
- [6] Heikkilä J. Geometric camera calibration using circular control points. *IEEE Trans Pattern Anal Mach Intell* 2000;22(10):1066–77.
- [7] Zhang ZY. A flexible new technique for camera calibration. *IEEE Trans Pattern Anal Mach Intell* 2000;22(11):1330–4.
- [8] Meng XQ, Li H, Hu ZY. A new easy camera calibration technique based on circular points. In: *Proceedings of the 11th British machine vision conference*; 2000; p. 496–05.
- [9] Zhang ZY. Camera calibration with one-dimensional objects. *IEEE Trans*

- Pattern Anal Mach Intell 2004;26(7):892–9.
- [10] Fei Q, Li QH, Luo YP, Hu DC. Camera calibration with one-dimensional objects moving under gravity. *Pattern Recognit* 2007;40(6):1785–92.
 - [11] Zhang H, Wong KK, Zhang GQ. Camera calibration from images of sphere. *IEEE Trans Pattern Anal Mach Intell* 2007;29(3):499–503.
 - [12] Wong KK, Zhang GQ, Chen ZH. A stratified approach for camera calibration using spheres. *IEEE Trans Image Process* 2011;20(2):305–16.
 - [13] Agrawal M, Davis L. Camera calibration using spheres: a semi-definite programming approach. In: *Proceedings of IEEE international conference on computer vision*, 2003, pp.782–789.
 - [14] Zhou FQ, Zhang GJ, Wei ZZ. Calibrating binocular vision sensor with one-dimensional target of unknown motion. *Chin J Mech Eng* 2006;42(6):92–6.
 - [15] Dawson DN, Birchfield ST. An energy minimization approach to automatic traffic camera calibration. *IEEE Trans Intell Transp Syst* 2013;14(3):1095–108.
 - [16] Zheng Y, Peng S. A practical roadside camera calibration method based on least squares optimization. *IEEE Trans Intell Transp Syst* 2014;15(2):831–43.
 - [17] Tian L, Zhu W, Li K, Yang Y. A camera calibration method for large field vision metrology. In: *Proceedings of the IEEE international conference on mechatronics and automation*. Beijing, China: 2015; p. 2632–637.
 - [18] Liu H, Wang C, Lu H, Yang W. Outdoor camera calibration method for a GPS & camera based surveillance system. In: *Proceedings of the IEEE international conference on industrial technology*, Viña del Mar, Chile: 2010; p. 263–67.
 - [19] Liang YJ, Miao YX, Chen XH, Sun ZY. Measuring method for contour of object in complex high temperature variation environment. In: *Proceedings of SPIE* 2013;8759:87590Z.
 - [20] Rodríguez J, Alanís F. Binocular self-calibration performed via adaptive genetic algorithm based on laser line imaging. *J Mod Optic* 2016.
 - [21] MORE J. The levenberg-marquardt algorithm, implementation and theory. In: Watson GA, editor. *Numerical analysis, lecture notes in mathematics*. Springer-Verlag; 1978. p. 105–16.
 - [22] J. Y. Bouguet, Camera calibration toolbox for Matlab, available from: (http://www.vision.caltech.edu/bouguetj/calib_doc/).
 - [23] Steger C. An unbiased detector of curvilinear structures. *IEEE Trans Pattern Anal Mach Intell* 1998;20(2):113–25.